Model identification and vision-based H_∞ position control of 6-DoF cable-driven parallel robots

Ryad Chellal, Loïc Cuvillon, Edouard Laroche

To appear in the *International Journal of Control*
Vol. 00, No. 00, Month 20XX, 1–23

Model identification and Vision-Based $\mathbf{H}_\infty$ Position Control of 6-DoF Cable-Driven Parallel Robots

R. Chellal, L. Cuvillon and E. Laroche

ICube, University of Strasbourg and CNRS, France
300 bd Sébastien Brant, CS 10413, F-67412 Illkirch Cedex, France

(*Revised version for review*)

This paper presents methodologies for the identification and control of 6-Degrees of Freedom (DoF) Cable-Driven Parallel Robots (CDPRs). First a two-step identification methodology is proposed to accurately estimate the kinematic parameters independently and prior to the dynamic parameters of a physics-based model of CDPRs. Second, an original control scheme is developed, including a vision-based position controller tuned with the $\mathbf{H}_\infty$ methodology and a cable tension distribution algorithm. The position is controlled in the operational space, making use of the end-effector pose measured by a motion-tracking system. A four-block $\mathbf{H}_\infty$ design scheme with adjusted weighting filters ensures good trajectory tracking and disturbance rejection properties for the CDPR system, which is a non-linear coupled MIMO system with constrained states. The tension management algorithm generates control signals that maintain the cables under feasible tensions. The paper makes an extensive review of the available methods and presents an extension of one of them. The presented methodologies are evaluated by simulations and experimentally on a redundant 6-DoF INCA 6D CDPR with 8 cables, equipped with a motion-tracking system.

Keywords: Cable-driven parallel robots; model identification; vision-based control ; H_∞ control; tension distribution

1. Introduction

Cable-Driven Parallel Robots (CDPRs) are special parallel robot manipulators where the end-effector or platform is connected to the base via cables only, its movement resulting from the winding and unwinding of the cables around pulleys actuated by motors. This kind of robot manipulator appeared in the late 80s by replacing the segments of the Gouth-Stewart platform manipulators by cables in order to solve the major problem of the reduced workspace of rigid parallel robots (Dagalakis et al., 1989).

Compared to serial and parallel manipulator robots actuated by rigid links, cable-actuated robots benefit from interesting features like: very large workspace, high speed motion due to the low moving mass, modular geometry, portability and adaptability to multi-scales. However, their control is a more complex issue as the cables must remain under tension at any time (Oh et Agrawal, 2005). The approaches available in the literature to solve this issue can be classified in two main categories. In the off-line solutions, a path planning step is used prior to motion in order to design a reference trajectory which guarantees that the cables remain under tension during the predefined motion (Gosselin, 2012; Trevisani, 2012). In the on-line solutions, an algorithm of tension distribution (also known as force calculation or redundancy resolution) is used to ensure that the control signals maintain the cable tensions inside a predefined feasible workspace during motion (Lafourcade, 2004;

Corresponding author. Email: laroche@unistra.fr

Ming and Higuchi, 1994). This is a common solution for redundant manipulators, where the number of cables exceeds the number of Degrees of Freedom (DoF) of the end-effector, and it is the solution considered in this work.

Dealing with position control of CDPR manipulators, most of the proposed methods rely on joint position measurements. According to the coordinate space chosen to solve this control problem, there are two alternatives. In the first one, the controllers are designed in the joint space coordinates. Using the Inverse Position Kinematic Model (IPKM), the reference end-effector pose is converted into reference joint positions which are then controlled by a feedback loop. Some related works are the joint space PD controller proposed by Kawamura et al. (2000) applied to the SEGESTA robot and later to the KNTU robot by Gholami et al. (2008), and the joint space PID controller for the redundant suspended ReelAx8 prototype presented by Lamaury et al. (2012a). In the second one, the controllers are designed in the task space coordinates. Assuming that a Direct Position Kinematic Model (DPKM) is available, the end-effector pose is calculated from the joint position measurements and a feedback control allows to track a reference pose. Gholami et al. (2008) evaluated such a task space PD controller and compared it to the previous approach. However, for parallel manipulators, the DPKM is difficult to obtain (see for instance Carricato et Merlet (2011) for an intensive study on the matter). In the previously mentioned control schemes, the modelling errors and the deformations of the cables result directly in errors on the end-effector pose. One solution for improving the accuracy is then to use some exteroceptive sensors in order to obtain a direct measurement of the end-effector pose. Some preliminary works using cameras have been proposed by Dallej et al. for controlling the redundant suspended ReelAx8 robot (2011) or the large-dimension CoGiRo robot (2012) .

CDPRs are non-linear coupled MIMO systems with constrained states. For such systems, stability issues arise with linear LTI or model inversion based controller as soon as the model is not well known or when the parameters evolve during operation. Multi-variable control methodologies that have been developed since the 90s now allow to manage the trade-off between performances and robustness and are then good candidates for CDPRs. Some preliminary results were proposed by Laroche et al. (2012) for the design of a LTI robust controller that manages both position and tension, including simulation results of a 3-DoF cable-robot with 4 cables.

The purpose of this paper is twofold. First, a two-step methodology is proposed to accurately estimate the kinematic parameters prior and independently from the dynamic parameters of a physics-based CDPRs model. It requires both the measurement of the motors angular positions (measured by optical encoders) and the end-effector pose (provided by a system of cameras). After a presentation of the available identification methods, experimental results are provided, showing that the identified model fits the system behaviour with good accuracy, and can then be used for control. Second, an original control scheme is developed in two parts: a vision-based position control scheme, for which an $\mathbf{H}_\infty$ methodology is proposed, in addition to a cable tension distribution management algorithm. The position control is achieved in the operational space, making use of an end-effector pose directly measured by a vision-tracking system. A four-blocks $\mathbf{H}_\infty$ design scheme with adjusted weighting filters ensures good trajectory tracking and disturbance rejection for CDPR systems which are Non-Linear Time Invariant (NLTI) coupled MIMO systems with constrained states. In conjunction with this position control loop, a tension management algorithm aims at ensuring that the control signals maintain the cables under feasible tensions. The paper makes an extensive review of the available methods and presents an algorithm inspired from one of them, to account for the motor dynamics. Results from simulations and experiments are then reported using the redundant 6-DoF CDPR INCA 6D prototype with 8 cables manufactured and sold by Haption, equipped with a motion-tracking system Bonita developed by Vicon.

The paper is organised as follows: Section 2 describes the setup composed of the INCA robot and the Bonita motion-capture system. In Section 3, a physics-based model of the 6-DoF CDPRs is developed. In Section 4, the identification methodology is described and implemented. Section 5 is dedicated to the control strategies and includes both simulation and experimental results.

2. System description

2.1 *INCA robot*

The INCA robot developed by Haption is a haptic device with force feedback that is used in this work as a manipulator to address the control issues raised by CDPRs.

On its 6D version, the INCA 6D has a cubic configuration of 3 m by side, and uses eight driving cables to move the end-effector and 8 balancing cables to ensure pretension in the driving cables when the motors are non-powered (Fig. 1(b)). Each actuator located at one of the eight vertices of the workspace (Fig. 1(a)) is composed of a DC motor with a current driver, coupled to both the driving and balancing winches (Fig. 1(b)) to store the cables, and is associated with a pulley to guide the cables, thus avoiding shearing. The contact points between the driving cables and the end-effector are called *attachment points*, and the contact points between the driving cables and the pulleys are called *output points*.

A measurement of the motor positions and currents are respectively achieved by incremental optical encoders and current sensors.

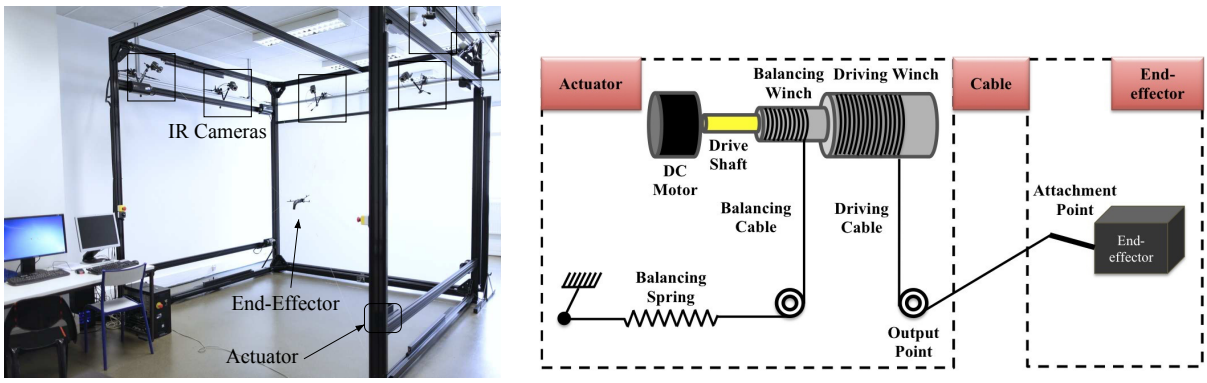

(a) The INCA robot and the 6 Bonita IR cameras for tracking of the robot end-effector

(b) Actuation scheme

Figure 1. The INCA robot

2.2 *Bonita motion-capture system*

The Bonita motion-capture system used to measure the pose of the INCA end-effector is composed of six infrared (IR) cameras (Fig. 1(a)) and a tracker software running on a Windows PC, both from Vicon company. Each camera has its own emitting source and delivers a grayscale image with VGA resolution up to a 250 Hz frame-rate. Assuming that this stereo system has been previously calibrated, the pose of the INCA end-effector fitted with five retro-reflective fixed markers can be tracked by the software.

The temporal and spatial performances of the pose reconstruction are critical for the robot control and have been evaluated as follows:

- the delay between the start of the image acquisition and the availability of the pose measurement has been evaluated at 10.7 ± 0.7 ms with a 200 Hz camera frame rate. This latency of roughly twice the acquisition period is the sum of one period of image acquisition and one period for the pose reconstruction.
- the accuracy of the pose is of 1.7 ± 0.4 mm. It has been estimated by the RMS error in the IR camera images between the current position of the visible markers and their expected positions given by the reconstructed pose of the end-effector.

2.3 *Real-time control architecture*

To allow the controller to operate at a higher frequency than the frequency of the Bonita motion-capture system, the control architecture summed up in Fig. 2 is designed as the following two asynchronous real-time tasks:

- the main periodic task is run by a PC under RT Linux at 1 kHz. It consists in reading the motor currents and the motor positions, checking the consistency of the robot state and finally computing the reference for the motor currents.
- a secondary task is run by a PC under Windows asynchronously at 200 Hz. It waits for the availability of the end-effector pose provided by the vision-tracking system.

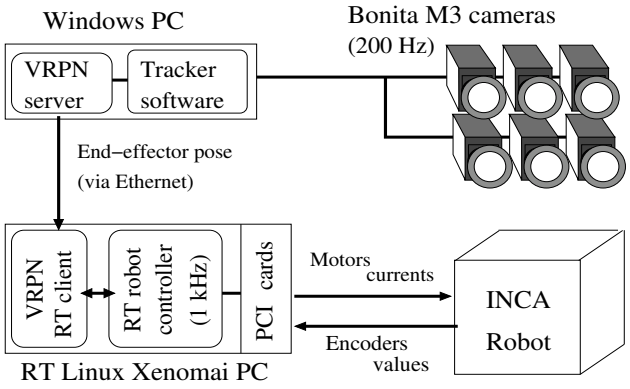

Figure 2. Real-time control architecture

3. Modelling of the 6-DoF CDPRs

The physics-based model considered in this work is derived from the general model for the m-DoF CDPR manipulators with n cables, which is augmented with the pretension system (balancing cables, winches and springs) of the INCA prototype. It is assumed that the cables are of negligible mass (straight, no sagging) and of infinite stiffness (inextensible).

3.1 *Kinematics modelling*

3.1.1 Position kinematics

Denoting $\mathcal{R}_o$ the base reference frame and $\mathcal{R}_e$ the end-effector frame centred at its center of mass, the pose of the end-effector can be represented by the vector $X_e = [P_e^T \ \Phi_e^T]^T$, with P_e the position of the origin and Φ_e a representation of the orientation of $\mathcal{R}_e$ with respect to the base reference frame $\mathcal{R}_o$ (Fig. 3(a)). Considering $\Phi_e = [\phi_r \ \phi_p \ \phi_y]^T$, the rotation matrix ${}^oR_e$ from $\mathcal{R}_o$ to $\mathcal{R}_e$ has been chosen as a composition of three successive rotations Roll-Pitch-Yaw (Khalil, 1999) of angles (ϕ_r, ϕ_p, ϕ_y) respectively around the principal axes (X_o, Y_o, Z_o) of $\mathcal{R}_o$:

$$ {}^oR_e(\Phi_e) = \begin{bmatrix} c_y c_p & c_y s_p s_r - s_y c_r & c_y s_p c_r + s_y s_r \\ s_y c_p & s_y s_p s_r + c_y c_r & s_y s_p c_r - c_y s_r \\ -s_p & c_p s_r & c_p c_r \end{bmatrix} \tag{1} $$

with $s_k = \sin\phi_k$ and $c_k = \cos\phi_k$, k standing for r, p or y.

The attachment point E_i with coordinates ${}^e r_i$ fixed in $\mathcal{R}_e$ is located at the position $P_{E_i} = P_e + {}^o R_e(\Phi_e)\, {}^e r_i$ in $\mathcal{R}_o$. With P_{O_i} denoting the position of an output point O_i fixed in $\mathcal{R}_o$, the length of cable $\#i$ writes $L_i(X_e) = \parallel l_i(X_e) \parallel_2$ where $l_i(X_e) = P_e + {}^o R_e(\Phi_e)\, {}^e r_i - P_{O_i}$. We then stack the lengths of the cables in $L = [L_1 \ \dots \ L_n]^T$.

By convention, the angular position is considered as increasing during winding. With a null reference of the motor positions $\theta_o = \mathbb{O}_{8\times 1}$ for the initial pose of the end-effector $X_{eo} = [P_{eo}^T \ \Phi_{eo}^T]^T$, the Inverse Position Kinematic Model (IPKM) is then given by:

$$\theta(X_e, \alpha_K) \ = \ -R_{pm}^{-1} \left(L(X_e, \alpha_K) - L(X_{eo}, \alpha_K)\right) \tag{2}$$

where α_K is the vector of the parameters involved in the kinematic model and $R_{pm} = \mathrm{diag}(r_{pm1_1}, ..., r_{pm1_n})$ contains the radii of the driving winches.

3.1.2 Velocity kinematics

Differentiating Eqn. (2) with respect to time yields the Inverse Velocity Kinematic Model (IVKM):

$$\dot{\theta} = -R_{pm}^{-1}\, J(X_e)\, V_e \tag{3}$$

where the i^{th} row of the inverse kinematics Jacobian matrix J is the same as for a rigid parallel manipulator (Merlet, 1997) and is given by $J_i(X_e) = [{u_i}^T(X_e) \ (r_i(\Phi_e) \times u_i(X_e))^T]$, in which $u_i(X_e) = l_i(X_e) \,/\, L_i(X_e)$ is the unit direction vector of the i^{th} driving cable (Fig. 3(a)). The end-effector velocity $V_e = [v_e^T \ w_e^T]^T$ (including the linear v_e and angular w_e velocities) can then be converted into the time derivative of end-effector pose $\dot{X}_e$ by:

$$V_e = A_v(\Phi_e)\, \dot{X}_e \tag{4}$$

with $A_v(\Phi_e) = \mathrm{diag}(\mathbb{I}_{3\times 3}, J_{rpy}(\Phi_e))$, in which the matrix J_{rpy} maps the angular velocity w_e to the time derivative of the chosen orientation representation $\dot{\Phi}_e$ such as $w_e = J_{rpy}(\Phi_e)\, \dot{\Phi}_e$. For a Roll-Pitch-Yaw representation of the rotation, J_{rpy} has the following form:

$$J_{rpy}(\Phi_e) = \begin{bmatrix} c_y\, c_p & -s_y & 0 \\ s_y\, c_p & c_y & 0 \\ -s_p & 0 & 1 \end{bmatrix} \tag{5}$$

Denoting $\tilde{J}(X_e) = R_{pm}^{-1}\, J(X_e)\, A_v(\Phi_e)$ and recalling the dependance with respect to the kinematic parameter vector α_K, the IVKM is finally rewritten as:

$$\dot{\theta} \ = \ -\tilde{J}(X_e, \alpha_K)\, \dot{X}_e \tag{6}$$

3.2 *Dynamics modelling*

3.2.1 End-effector dynamics

The Newton-Euler equations (Khalil, 1999) applied to the end-effector rigid body of mass M_e and moment of inertia tensor I_e, written at its center of mass O_e gives:

$$F_e = A_e(\Phi_e)\, \dot{V}_e + B_e(\Phi_e, \dot{\Phi}_e) \tag{7}$$

with $A_e(\Phi_e) = \begin{bmatrix} M_e\,\mathbb{I}_{3\times3} & \mathbb{O}_{3\times3} \\ \mathbb{O}_{3\times3} & {}^oI_e(\Phi_e) \end{bmatrix}$ and $B_e(\dot{\Phi}_e, \Phi_e) = \begin{bmatrix} \mathbb{O}_{3\times1} \\ w_e(\Phi_e, \dot{\Phi}_e) \times ({}^oI_e(\Phi_e)\, w_e(\Phi_e, \dot{\Phi}_e)) \end{bmatrix}$, in which the moment of inertia tensor ${}^oI_e$ expressed in $\mathcal{R}_o$ is calculated from its constant tensor ${}^eI_e$ expressed in $\mathcal{R}_e$ such as: ${}^oI_e(\Phi_e) = {}^oR_e(\Phi_e)\,{}^eI_e\,{}^oR_e^T(\Phi_e)$.

The resulting wrench $F_e = [f_e^T\ m_e^T]^T$ (including the forces f_e and moments m_e) applied on the end-effector center of mass O_e includes contributions of the cables tensions $T = [T_1\ \dots\ T_n]^T$ applied on the end-effector side (Fig. 3(a)) and of the weight G:

$$F_e = W(X_e)\,T + G \tag{8}$$

where $W(X_e) = -J^T(X_e)$ is the wrench matrix and $G = [0\ 0\ -M_e\,g\ 0\ 0\ 0]^T$ with g the modulus of the gravity acceleration vector.

3.2.2 Actuators dynamics

With the diagonal matrix of the inertia moments $J_{eq} = j_{eq}\mathbb{I}_n$, viscous $F_{veq} = f_v\mathbb{I}_n$ and Coulomb $F_{ceq} = f_c\mathbb{I}_n$ friction coefficients, rotational stiffness K_{eq} of the balancing spring, and neglecting the tension loss due to the output roll ($T_a = T_e = T$ in Fig.3(b)), the equation of the actuator dynamics writes:

$$J_{eq}\,\ddot{\theta} + F_{veq}\,\dot{\theta} + F_{ceq}\,\mathrm{sign}(\dot{\theta}) + K_{eq}\,\theta \;=\; K_{em}\,I_m - R_{pm}\,(T_a - T_{ao}) \tag{9}$$

with:

- $K_{eq} = K_{sp}\,{R_{pe}}^2$, $R_{pe} = r_{pe}\mathbb{I}_n$ being the diagonal matrix of the balancing winches radius and K_{sp}, the diagonal matrix of the balancing spring stiffness,
- $K_{em} = k_{em}\mathbb{I}_n$, a diagonal matrix with the torque constants,
- $I_m = [I_{m1}, \dots, I_{mn}]^T$ the motor current vector related to the motor torque vector $\tau_m = [\tau_{m1}\ \dots\ \tau_{mn}]^T$ by the linear equation $\tau_m = K_{em}\,I_m$,
- and $T_{ao} = K_{eq}\,R_{pm}^{-2}\,L(X_{e_o})$ the pretension of the driving cables for an initial pose X_{e_o} of the end-effector, due to a change of length of the balancing springs by $R_{pe}R_{pm}^{-1}L(X_{e_o})$.

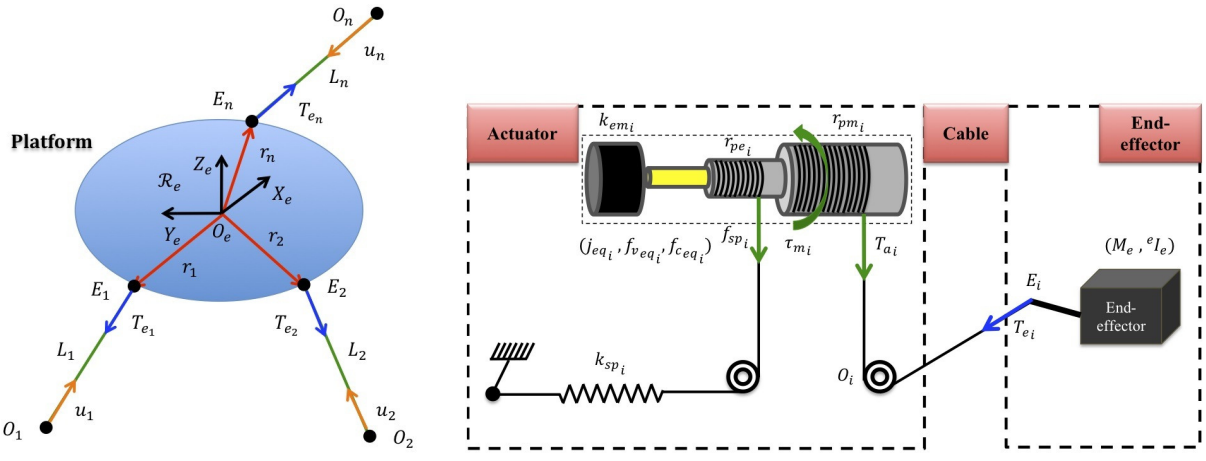

(a) End-effector (b) Actuator

Figure 3. Diagram of the 6-DoF CDPR with the dynamic parameters

3.2.3 System dynamics

Combining (7), (8), (9) with the use of Eqn. (2), (4), Eqn. (6) and their time derivative, the Direct Dynamic Model (DDM) of the system written in the operational space is given by:

$$M_x(X_e)\,\ddot{X}_e + C_x(X_e,\dot{X}_e)\; + K_x(X_e)\; + G_x \;\; = \;\; A_v^T(\Phi_e)\,F_{ev} \tag{10}$$

under the n constraints expressing that the cables are kept inside a feasible tensions workspace $[T_{\min}\ T_{\max}]$:

$$T_{\min} \;\leq\; T(I_m,\theta,\dot{\theta},\ddot{\theta}) \;\leq\; T_{\max} \tag{11}$$

The matrices involved in the model write:

$$\left\{\begin{array}{ll} M_x(X_e) & = A_v^T(\Phi_e)\,A_e(X_e)\,A_v(\Phi_e) + \tilde{J}^T(X_e)\,J_{eq}\,\tilde{J}(X_e) \\ K_x(X_e) & = \tilde{J}^T(X_e)\,K_{eq}\,R_{pm}^{-1}\,L(X_e) \\ G_x & = -A_v^T(\Phi_e)\,G = -G \\ C_x(X_e,\dot{X}_e) & = \Big[A_v^T(\Phi_e)\,A_e(X_e)\,\dot{A}_v(\Phi_e,\dot{\Phi}_e)\; + \tilde{J}^T(X_e)\,F_{veq}\,\tilde{J}(X_e)\; + \tilde{J}^T(X_e)\,J_{eq}\,\dot{\tilde{J}}(X_e,\dot{X}_e)\Big]\,\dot{X}_e \\ & \quad + A_v^T(\Phi_e)\,B_e(\Phi_e,\dot{\Phi}_e)\; + \tilde{J}^T(X_e)\,f_{ceq}\,\mathrm{sign}(\tilde{J}(X_e)\dot{X}_e) \end{array}\right. \tag{12}$$

and the wrench F_{ev} resulting from the motor-current vector I_m is:

$$F_{ev} = W_I(X_e)\,I_m \tag{13}$$

where $W_I(X_e) = W(X_e)\,R_{pm}^{-1}\,K_{em}$. This model relies on the kinematic parameters stacked in α_K and also on the dynamic parameters (inertias, torque constant, friction ratios...) stacked in α_D.

3.2.4 Nominal linear model

As can be seen in the system dynamics given by the ODEs system (10), CDPRs are NLTI coupled MIMO systems. So the linearisation of (10) is required for the use of the $\mathbf{H}_\infty$ methodology presented in Section 5. It leads to the linear coupled ODEs system:

$$M_o\,\delta\ddot{X}_e + C_o\,\delta\dot{X}_e + K_o\,\delta X_e = A_v^T(\Phi_{e_o})\,\delta F_{ev} \tag{14}$$

where the linearised dynamic matrices could be evaluated analytically by differentiating F_{ev} from (10) at the operating point $op = (X_{e_o}, \dot{X}_{e_o}, \ddot{X}_{e_o})$:

$$M_o = \left.\frac{\partial(A_v^T\,F_{ev})}{\partial\ddot{X}_e}\right|_{op} \quad C_o = \left.\frac{\partial(A_v^T\,F_{ev})}{\partial\dot{X}_e}\right|_{op} \quad K_o = \left.\frac{\partial(A_v^T\,F_{ev})}{\partial X_e}\right|_{op} \tag{15}$$

and are expressed at the operating or equilibrium point $op = (X_{e_o}, 0, 0)$ by:

$$\left\{\begin{array}{ll} M_o & = A_v^T(\Phi_{e_0})A_e(X_{e_0})A_v(\Phi_{e_0}) + \tilde{J}^T(X_{e_o})\,J_{eq}\,\tilde{J}(X_{e_o}) \\ C_o & = \tilde{J}^T(X_{e_o})\,F_{veq}\,\tilde{J}(X_{e_o}) \\ K_o & = \tilde{J}^T(X_{e_o})\,K_{eq}\,\tilde{J}(X_{e_o}) + \left[\left.\frac{\partial\tilde{J}^T}{\partial p_x}\right|_{X_{e_o}} K_{eq}\,R_{pm}^{-1}\,L(X_{e_o}) \;\middle|\; \ldots \;\middle|\; \left.\frac{\partial\tilde{J}^T}{\partial\phi_y}\right|_{X_{e_o}} K_{eq}\,R_{pm}^{-1}\,L(X_{e_o})\right] \end{array}\right. \tag{16}$$

Coulomb frictions are naturally removed in the linear model. They can be considered as disturbances acting on the wrench that will be rejected by the controller.

Hence, the state-space representation of the linearised system based on state $x = [\delta X_e^T \ \delta \dot{X}_e^T]^T \in \mathbb{R}^{12}$, control $u = \delta F_{e_v} \in \mathbb{R}^6$ and measurement $y = \delta X_e \in \mathbb{R}^6$ vectors writes:

$$\left\{ \begin{array}{ll} \dot{x} & = A_o \, x + B_o \, u \\ y & = C_o \, x + D_o \, u \end{array} \right. \tag{17}$$

with the state-space matrices expressed as $A_o = \begin{bmatrix} \mathbb{O}_{6\times6} & \mathbb{I}_{6\times6} \\ -M_o^{-1} \, K_o & -M_o^{-1} \, C_o \end{bmatrix}$, $B_o = \begin{bmatrix} \mathbb{O}_{6\times6} \\ M_o^{-1} \, A_v^T(\Phi_{e_o}) \end{bmatrix}$, $C_o = \begin{bmatrix} \mathbb{I}_{6\times6} & \mathbb{O}_{6\times6} \end{bmatrix}$ and $D_o = \mathbb{O}_{6\times6}$.

4. Model identification

A number of approaches are available in the literature for identification of robot models. Yu et al. (2011) have considered the estimation of the kinematic parameters of a rigid parallel manipulator. For estimation of dynamic parameters, the reader can refer to Gautier and Poignet (2002); Gautier et al. (2013) for the electromechanics systems in general and for the serial robots particularly and to Poignet et al. (2003) for the case of parallel robots.

4.1 *Identification methodology*

Following Renaud et al. (2006), we propose to estimate the parameters sequentially in two steps, thus reducing the number of parameters to be considered at one time:

- **Step 1**: The kinematic parameters are first estimated using the IPKM (see Vischer and Clavel (1998) for an example of determination of the kinematic parameters of a parallel robot).
- **Step 2**: The dynamic parameters are then estimated from the DDM, using the identified kinematic parameters.

4.1.1 Step 1: Kinematic parameters identification

Considering a set of N_s measurements, the estimate $\widehat{\alpha}_K$ of the vector α_K of the kinematic parameters can be determined by minimising the following criterion $E(\alpha_K)$ on the motor positions (see Fig. 4.a):

$$E(\alpha_K) = \sum_{i=1}^{n} \sum_{k=1}^{N_s} \left(\theta_{ik} - \widehat{\theta}_{ik}(\alpha_K) \right)^2 \tag{18}$$

with :

θ_{ik}	$= \theta_i(t = k\,T_s)$	motor position measurements.
$\widehat{\theta}_{ik}(\alpha_K)$	$= \widehat{\theta}_i(t = k\,T_s, \alpha_K)$	motor position estimations using the IPKM.

Minimising $E(\alpha_K)$ is a non-linear least squares optimisation problem that can be solved iteratively using numerical algorithms such as: Gradient-Descendant, Gauss-Newton or Levenberg-Marquardt. Denoting σ_θ^2 the variance of the measurement error on the joint positions and A the sensitivity

matrix of the model of dimension $nN_s \times n_{\alpha_K}$

$$A = \begin{bmatrix} \frac{d\hat{\theta}_{11}}{d\alpha_K} \\ \vdots \\ \frac{d\hat{\theta}_{nN_s}}{d\alpha_K} \end{bmatrix} \tag{19}$$

the covariance matrix of the error on the estimates writes $\Sigma^2_{\alpha_K} = \sigma^2_\theta (A^T A)^{-T}$ (Walter and Pronzato, 1997).

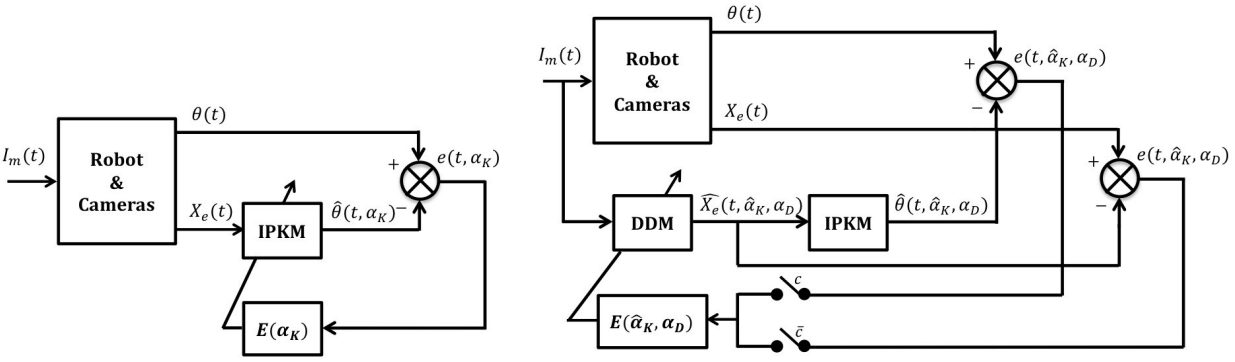

(a) Kinematic parameter estimation scheme (b) Dynamic parameter estimation scheme

Figure 4. Parameter estimation schemes

4.1.2 Step 2: Dynamic parameters identification

The identification of the dynamic parameters of a robot is a general complex problem, due to the non-linear nature of both the input-output behaviour and the parameter dependence of these MIMO systems. Identification methodologies for robots can be classified according to the minimization criterion (Gautier et al., 2013):

- **Inverse Dynamic Identification Model (IDIM)**: the Inverse Dynamic Model (IDM) is written in a linear form according to the parameters to be estimated, thus allowing to compute their estimate in one shot by minimizing the quadratic error between the measured input and its estimation computed on the same output trajectory (Gautier and Poignet, 2002). This method requires the estimation of the speed and the acceleration, through bandpass filtering of the joint position at high sampling rate.
- **Output Error (OE)**: the quadratic error between measured outputs and their estimate is minimised, where the output estimate is computed with the DDM, the system being fed with the same input signal. This technique can be implemented in an open-loop (OLOE) or closed-loop (CLOE) situations (Janot et al., 2014). This very popular method often yields to a non-convex problem with possible local minima and is then sensitive to initialisation.

Despite of its drawbacks, the OE method has been chosen as it is more realistic (the errors are mainly on the measurement signals) and thus leads to a more accurate model for control synthesis. Beneficing from the stabilization effect of the balancing springs, the experiments were done in open loop. For a robot without balancing springs, a closed-loop framework would better suit to ensure that the platform remains within a limited workspace. An excitation is first designed, leading to a set of input and output data collected from N_s samples at a sampling rate f_e. Then, the estimate $\widehat{\alpha}_D$ of the vector α_D of the dynamic parameters can be determined by minimising the following dynamic

identification error criterion $E(\widehat{\alpha}_K, \alpha_D)$, defined in the operational space in term of end-effector posture (see Fig. 4.b with $c = 0$):

$$E(\widehat{\alpha}_K, \alpha_D) = \sum_{i=1}^{6} \sum_{k=1}^{N_s} \left(X_{eik} - \widehat{X_{eik}}(\widehat{\alpha}_K, \alpha_D)\right)^2 \tag{20}$$

or also in the joint space in term of motors positioning (see Fig. 4.b with $c = 1$):

$$E(\widehat{\alpha}_K, \alpha_D) = \sum_{i=1}^{n} \sum_{k=1}^{N_s} \left(\theta_{ik} - \widehat{\theta}_{ik}(\widehat{\alpha}_K, \alpha_D)\right)^2 \tag{21}$$

with :

X_{eik}	$= X_{ei}(t = k\,T_s)$	end-effector pose measurement,
$\widehat{X_{eik}}(\widehat{\alpha}_K, \alpha_D)$	$= \widehat{X_{ei}}(t = k\,T_s, \widehat{\alpha}_K, \alpha_D)$	end-effector pose estimation using the DDM,
θ_{ik}	$= \theta_i(t = k\,T_s)$	motor position measurements,
$\widehat{\theta}_{ik}(\widehat{\alpha}_K, \alpha_D)$	$= \widehat{\theta}_i(t = k\,T_s, \widehat{\alpha}_K, \alpha_D)$	motor position estimations using the DDM and IPKM.

As for the kinematic parameters, minimising $E(\widehat{\alpha}_K, \alpha_D)$ is a non-linear least-square optimisation problem that can be solved iteratively using the same algorithms mentioned for the kinematic parameters estimation. However, the evaluation of the objective function requires the simulation of the DDM, which is very demanding in computation time.

4.2 *Implementation and results*

The proposed identification methodology has been implemented on the INCA 6D CDPR. For the i^{th} output of a MIMO system of input vector u ($\dim(u) = N_u$) and output vector y ($\dim(y) = N_y$) among a set of N_s samples, the fit is defined by:

$$FIT_i(\%) = \left(1 - \frac{\sum_{i=1}^{N_y} \sum_{k=1}^{N_s} (y_{ik} - \widehat{y}_{ik})^2}{\sum_{i=1}^{N_y} \sum_{k=1}^{N_s} (y_{ik} - \overline{y}_i)^2}\right) \times 100 \tag{22}$$

where $\widehat{y}$ is the estimation of the output vector y and $\overline{y}_i$ the average of the i^{th} output y_i.

4.2.1 Initial values of the parameters

The reference frame $\mathcal{R}_o$ is located at the center of the workspace (Fig. 5(a)), and the initial position for the frame $\mathcal{R}_e$ attached to the end-effector is chosen equal to $\mathcal{R}_o$ (Fig. 5(b)).

Each motor is controlled in current and the current loop, i.e. the transfer between the current reference I^*_{mi} and the effective motor current I_{mi}, is modelled by a continuous-time first-order transfer function $G_i(s) = 1\,/\,(1 + \tau_i\, s)$ with a time constant τ_i.

The initial values of the kinematic (Fig. 5) and dynamic parameters of the INCA 6D robot, known by design or calculated, are given in the Table 1. The different actuators are assumed to have the same parameters.

Coulomb friction parameter f_{ceq} has been evaluated by powering each motor separately with a ramp signal for the reference current slowly varying from $I_{\min} = 0$ A to $I_{\max} = 3$ A with a slope of 1 A/s, whereas the other motors are controlled to 0 A. The Coulomb friction coefficient is then calculated when detecting the minimum value of the current that produces a motion of the end-effector. The worse case over the 8 winders has been considered for f_{ceq} given in Tab. 1.

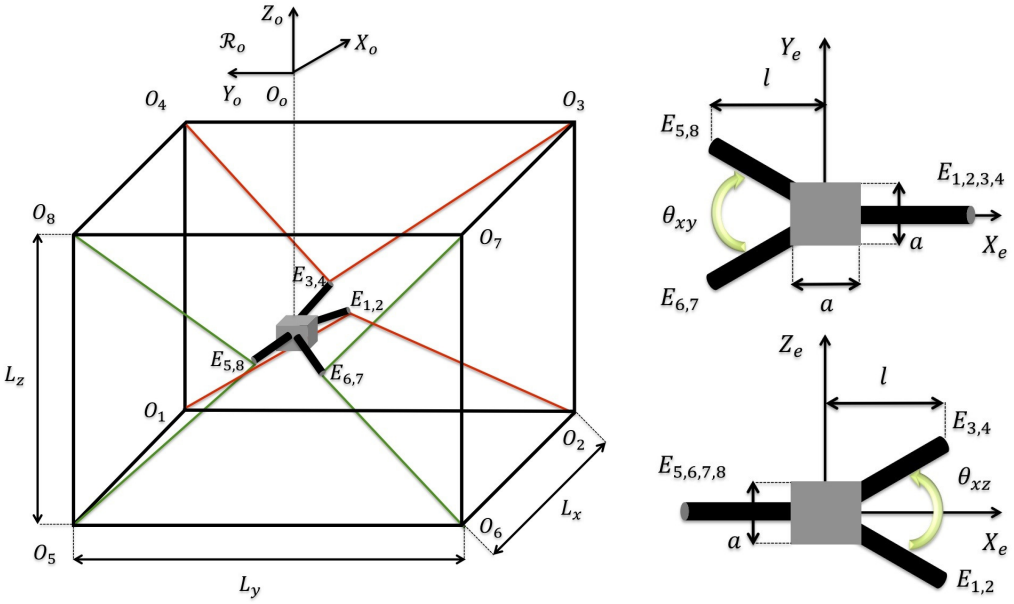

(a) Workspace (b) End-effector

Figure 5. Kinematic parameters of the INCA 6D robot

4.2.2 Estimation of the kinematic parameters

The test consists in moving the effector in eight different directions by applying successively a current reference of 1 A on one motor and 0 A on the other ones. The positions of the motors and the pose of the end-effector are acquired at steady-state.

The identification scheme presented in subsection 4.1.1 and summarised in Fig. 4(a) has been implemented using the Levenberg-Marquardt optimiser. The estimates of the kinematic parameters are given in Table 1. Notice that parameters a and r_{pe} are not involved in the kinematics modelling and then were not involved in the estimation procedure. The comparison between the positions of the motors estimations issued from the IPKM and the experimental identification data is shown in Fig. 6. The error on the motor position is centered (less than 0.4°, i.e. about 1 mm on the cable length) and the standard deviation is 45°, corresponding to 13.7 mm on the cable length. The standard deviation of the errors on the estimates provided in Table 1 are computed from the diagonal terms of $\Sigma^2_{\alpha_K}$.

The corresponding numerical values of the fit (22) on the motors positions are provided in the first column of the Table 2. One can notice that the model reproduces accurately the measured positions.

4.2.3 Estimation of the dynamic parameters

4.2.3.1 Experiment. The choice of the excitation trajectories is an important point for the identification procedure. Indeed, the model needs not only to be structurally identifiable, but the excitation trajectory must also be rich enough. The excitation trajectories must contain both slow (for friction and stiffness) and fast (for inertia) dynamics.

For the current case of a CDPR, the trajectories should be also large enough to excite the nonlinear behavior, the cable tension must be sufficiently high to avoid slackness, and sufficiently slow not to excite the vibrations of the cables.

Motor current signals have been chosen as decoupled Pseudo-Random Binary Sequence (PRBS) that are usually used in system identification as they can both excite the different inputs of a multivariable system in a decoupled fashion and are able to excite over a large bandwidth. For the

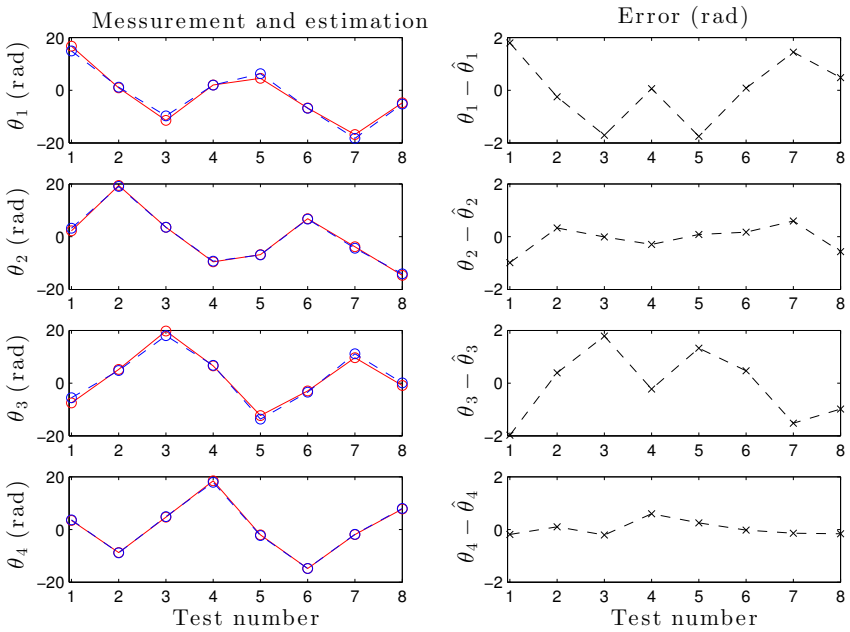

Figure 6. Estimation of the kinematic parameters. Left-hand side: experimental (plain line) and estimated (dashed line) angular position for the four first motors. Right-hand side: corresponding estimation errors

identification trajectory, the low level $I_{\min} = 0$ A and high level $I_{\max} = 1$ A of the signals are adjusted to respect the constraints on the cable tensions. The upper bound of the frequency band [0 $f_{\max}$] was set to $f_{\max} = 1$ Hz, during a time interval [0 5] s.

Cross validations have been performed with different PRBS trajectories, with additional data that were not used for training the model. Results are reported in Table 2. First, Val(a) is the continuation of the identification trajectory over [5 s - 10 s], thus obtained with the same tuning parameters. Then, Val(b) is obtained by varying the frequency $f_{\max}$; Val(c) by varying the current levels $I_{\min}$ and $I_{\max}$ and Val(d) by varying both of them. Notice that the average fit obtained with the initial values of the parameters was of 3.5 %. It reached 45 % when dividing the initial value of $f_{v_{eq}}$ by 10. These figures show that the parameter estimation step is paramount for improving the accuracy of the model.

The validation trajectories Val(e) and Val(f) with much higher frequency $f_{\max}$ allow to evaluate the effects of the cable vibrations that were observed during these experiments and that are not accounted for in the model.

4.2.3.2 Estimated dynamic parameters. Applying the dynamic identification scheme presented previously in Fig. 4(b) (considering the joint positions as outputs, i.e. with $c = 1$), the dynamic parameters are estimated iteratively using the Levenberg-Marquardt optimiser for solving the non-linear least-square optimisation problem of Eqn. (21).

The estimates of the dynamic parameters are given in Table 1. Parameters k_{em} and τ_i have been maintained at their initial values, that have been confirmed by previous experiments. The non-diagonal components of the moment of inertia are set to: ${}^eI_{exy} = {}^eI_{eyz} = {}^eI_{exz} = 0$ kg·m^2, and the diagonal components ${}^eI_{eyy}$ and ${}^eI_{ezz}$ are set as equal (${}^eI_{ezz} = {}^eI_{eyy}$), because of the symmetry of the end-effector.

An evaluation of the standard deviation of the estimates are given in the last column of table 1. This evaluation has been done by considering the sum of the parameter variances when considering all the errors on the kinematic parameters. More precisely, the dynamic parameter identification

has been run seven more times, considering an error of 1 % on each kinematic parameter, thus resulting in a sensitivity matrix expressing the effect of an error on each kinematic parameter on the dynamic parameter estimate. The variances of all the kinematic parameters, weighted by their sensitivities, are then summed up to produce the variances of the dynamic parameter estimates and finally their relative standard deviations given in table 1. One can notice that the highest deviations are for the inertias and are of 13 %.

Kinematic parameters	**Initial values**	**Est. values**	**STD** %
L_x (m)	2.53	2.50	6.8
L_y (m)	2.8	2.75	7.0
L_z (m)	3	3.05	5.4
a (mm)	41	41*	/
l (mm)	153	138	18.7
θ_{xy} (^{o})	70	63.0	0.6
θ_{xz} (^{o})	24	21.6	0.3
r_{pe} (mm)	6	6*	/
r_{pm} (mm)	17.5	17.5	1.0

Dynamic parameters	**Initial values**	**Estimated values**	**STD** %
M_e (kg)	0.157	0.289	0.3
${}^eI_{exx}$ (kg·m^2)	$4.97 \cdot 10^{-3}$	$1.49 \cdot 10^{-4}$	10.3
${}^eI_{eyy}$ (kg·m^2)	$6.91 \cdot 10^{-3}$	$2.07 \cdot 10^{-4}$	13.0
${}^eI_{ezz}$ (kg·m^2)	$6.91 \cdot 10^{-3}$	$2.07 \cdot 10^{-4}$	13.0
${}^eI_{exy}$ (kg·m^2)	0	0*	/
${}^eI_{eyz}$ (kg·m^2)	0	0*	/
${}^eI_{exz}$ (kg·m^2)	0	0*	/
j_{eq} (kg·m^2)	$2.91 \cdot 10^{-5}$	$3.88 \cdot 10^{-5}$	0.4
$f_{v_{eq}}$ ((N·m)/(rad/s))	$3.1 \cdot 10^{-3}$	$6.68 \cdot 10^{-5}$	3.8
$f_{c_{eq}}$ ((N·m)/(rad/s))	$1.8 \cdot 10^{-3}$	$4.4 \cdot 10^{-3}$	3.3
k_{sp} (N/m)	16	14.4	0.05
k_{em} ((N·m)/A)	$60.3 \cdot 10^{-3}$	$60.3 \cdot 10^{-3}$*	/
τ (ms)	1.3	no id.	/

Table 1. Initial and estimated values of the kinematic and dynamic parameters of the INCA 6D robot (∗: parameters that have been kept equal to their initial value)

In Fig. 7 are provided for the first three motors: the reference current (on the top), the estimated and measured motor angular positions (2nd row) and a zoom on the motor position error (lower row).

Table 2 provides the numerical values of the fit (22) on the motor positions. The fit obtained with the identification trajectory (see the column labeled "Dynamic ident") is complemented with the fit obtained for six different validation trajectories with variable amplitudes and frequencies. One can see that the model reproduces accurately the measurement, even on the validation data that were not used for identification. These results validate the assumptions used for deriving the model such as the negligible mass of the cables and their infinite stiffness.

4.2.4 Frequency-domain behaviour

The linearisation has been performed for the end-effector velocity and acceleration equal to zero. The nominal model corresponds to a position of the platform at the center of the workspace, with the nominal values of the kinematic and dynamic parameters previously estimated.

The frequency behaviour of the nominal linear model $G_n(s)$ is reported in Fig. 8. The singular values for both position and orientation models behave as a second order under-damped LTI system with a resonance at the frequencies close to 5 rad/s for position and of 22 rad/s for orientation.

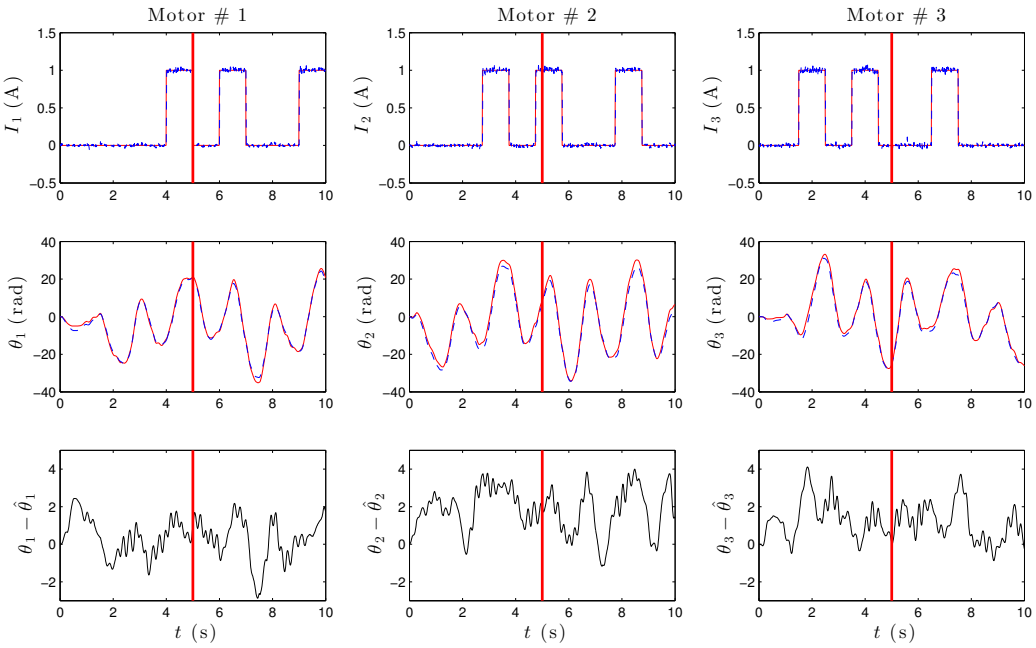

Figure 7. Identification and validation results of the dynamic model, for the first three motors (left to right). On the top: reference (plain line) and measured (dashed) values of the motor current; on the second row: predicted value (plain) and measured values (dashed) of the motor positions; lower row: motor prediction error. Before 5 s: data used for identification; after 5 s: validation data

PRBS parameters		**Dynamic Ident**	**Dynamic Val(a)**	**Dynamic Val(b)**	**Dynamic Val(c)**	**Dynamic Val(d)**	**Dynamic Val(e)**	**Dynamic Val(f)**
$I_{\min}$ (A)		0	0	0	0.5	0.5	0	0.5
$I_{\max}$ (A)		1	1	1	1.5	1.5	1	1.5
$f_{\max}$ (Hz)		1	1	2	1	2	5	5
Motors	**Kinematic Ident**	**Dynamic Ident**	**Dynamic Val(a)**	**Dynamic Val(b)**	**Dynamic Val(c)**	**Dynamic Val(d)**	**Dynamic Val(e)**	**Dynamic Val(f)**
Motor 1	88.6	91.2	92.5	84.8	86.1	90.1	83.3	82.2
Motor 2	88.2	85.1	88.0	84.8	81.4	86.8	69.9	69.3
Motor 3	85.7	88.2	89.1	82.6	81.5	82.6	80.4	77.9
Motor 4	92.9	93.9	93.4	88.2	85.7	89.1	79.3	74.1
Motor 5	88.9	86.8	84.7	77.9	82.0	82.6	79.9	79.7
Motor 6	84.1	93.6	92.0	87.1	85.4	89.3	81.3	75.9
Motor 7	83.4	90.3	90.5	83.7	86.0	88.8	83.0	82.0
Motor 8	95.1	85.7	87.8	82.1	84.3	87.0	70.9	72.0
Average	88.4	89.3	89.7	83.9	84.1	87.0	78.5	76.6

Table 2. Identification results: fit on the motors positions

5. Position control and tension distribution

The system can be considered as redundant as the number of actuators exceeds the number of DoF of the platform (refer to Kanoun et al. (2011) for a more general reflexion on redundant systems). The extra DoF are used to handle the cable tension. The considered control scheme presented in Fig. 9 is composed of two parts detailed in this section:

- **Position control** that aims to control the pose of the end-effector at a reference value. It is typically a dynamic position-based visual control scheme (also known as Position-Based Visual Servoing (PBVS) or 3D Visual Servoing (3DVS)).
- **Tension distribution** that aims to maintain the tension of the cables inside a feasible workspace.

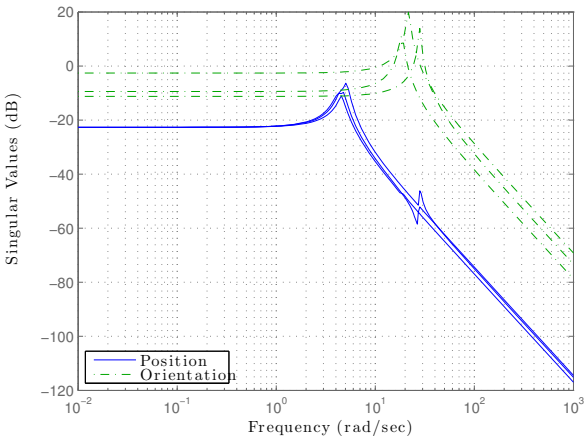

Figure 8. Singular values of the nominal model $G_n(s)$: position and orientation parts

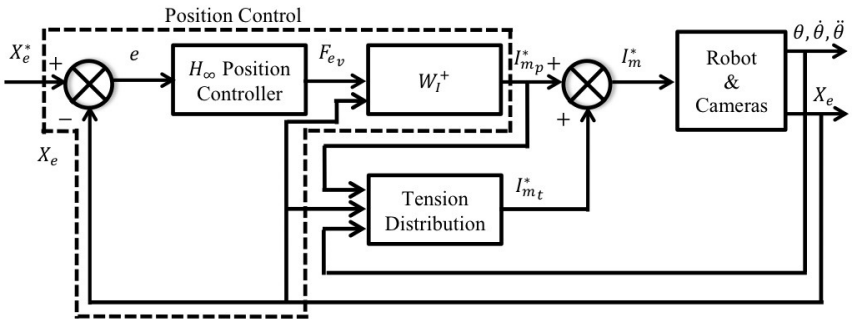

Figure 9. Control scheme

5.1 *Position control*

5.1.1 H_∞ synthesis

The $\mathbf{H}_\infty$ synthesis provides a framework for tuning dynamic output-feedback MIMO controllers in the frequency domain, allowing to handle easily the robustness versus performance trade-off (Duc and Font, 1999).

In the standard synthesis scheme described in Fig. 10, the controller $K(s)$ to be designed closes the loop of the extended plant $G_e(s)$, thus modifying the performance channel from v to z. Weighting filters located at the input ($W_i(s)$) and output ($W_o(s)$) complete the so-called augmented scheme.

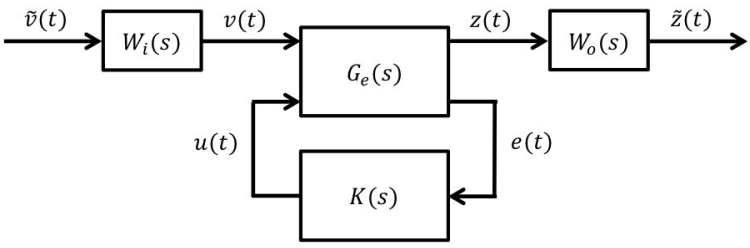

Figure 10. Standard $\mathbf{H}_\infty$ synthesis scheme with the extended plant $G_e(s)$, the weighting filters $W_i(s)$ and $W_o(s)$ and the controller $K(s)$

A number of problems can be recast into the following $\mathbf{H}_\infty$ synthesis problem that consists in computing $K(s)$ that:

- stabilises the weighted closed-loop system in Fig. 10;
- minimises $\gamma := \min_{K(s)} \| T_{\tilde{z}\tilde{v}}(s) \|_\infty$, i.e. the $\mathbf{H}_\infty$ norm[1] of the weighted closed-loop system $T_{\tilde{z}\tilde{v}}(s) = W_o(s)\, T_{zv}(s)\, W_i(s)$.

Assuming that the weighting filters $W_i(s)$ and $W_o(s)$ are diagonal, and denoting $W_i(s) = \text{diag}(W_{i1}(s), \ldots, W_{in_v}(s))$ and $W_o(s) = \text{diag}(W_{o1}(s), \ldots, W_{on_z}(s))$, where n_v and n_z being the dimensions of v and z respectively, then any SISO transfer $T_{z_k v_l}(s)$ between input v_k and output z_l satisfies:

$$|T_{z_k v_l}(j\omega)| \leq \frac{\gamma}{|W_{ol}(j\omega)| \cdot |W_{ik}(j\omega)|} \quad (\forall\, \omega \in \mathbb{R}^+) \tag{23}$$

Therefore, $\frac{1}{W_{ol}(s)W_{ik}(s)}$ is a template for the performance channel $T_{z_k v_l}(s)$ and the template is satisfied as soon as $\gamma \leq 1$.

The resolution of the standard problem of the $\mathbf{H}_\infty$ synthesis can be done by solving the resulted Riccati (Dolye et al., 1989) or LMI equations (Gahinet and Apkarian, 1994) resulting in full-order controllers, i.e. controllers with the same order as the augmented plant. Solvers are also available for the structured $\mathbf{H}_\infty$ synthesis: let us mention the HIFOO package (Burke et al., 2006) and `hinfstruct` available in the the Robust Control Toolbox (Apkarian et al., 2006).

To summarise, the method consists in the following steps:

- select the performance channels,
- design the weighting functions according to the requirements,
- compute the augmented plant and design the controller,
- iterate the two previous steps until γ is close to one.

5.1.2 Controller design

Fig. 11 depicts the synthesis scheme. The control scheme is deduced by ignoring the weighting filters $W_1(s)$, $W_2(s)$ and $W_3(s)$. It allows to control the measurement vector $y = X_e$ to the reference $r = X_e^*$, while rejecting the disturbance d that is added on the control vector u and considering the measurement noise b_m. As b_m and r have the same effects on the signals of interest e and u, only r is considered for building the extended plant $G_e(s)$, leading to a four-block design scheme equivalent to the scheme of Fig. 10 by selecting the signals $v = [r^T\ d^T]^T$ and $z = [e^T\ u^T]^T$, and the weighting filters $W_i(s) = \text{diag}(\mathbb{I}_{6\times 6}, W_3(s))$ and $W_o(s) = \text{diag}(W_1(s), W_2(s))$.

The weighing filters are chosen as following:

- $W_1(s)$ allows to tune the sensitivity function $S(s) = T_{er}(s)$, i.e. the transfer from r to e. It is chosen as constant, to impose the modulus margin Δ_M. As $\Delta_M = 1/||S(s)||_\infty$, we select $W_1(s) = \Delta_M^*$ where Δ_M^* denotes the required modulus margin.
- $W_2(s)$ allows to tune $T_{ur}(s)$, the transfer between r to u, which is equal to $T_{ub_m}(s)$. So $W_2(s)$ has the charge of reducing the effect of the measurement noise on the control signal. Thus, $W_2(s)$ must amplify in the high frequencies and $1/W_2(s)$ is chosen as a low-pass filter.
- $W_3(s)$ is used to penalise the disturbance in the low frequency thus enhancing the disturbance rejection properties.

The desired performances are: a bandwidth of 5 rad/s, a modulus margin of 6 dB and an accuracy of 10^{-3} due to d for both position and orientation, with a reasonable amplitude of the control inputs

[1]The $\mathbf{H}_\infty$ norm of a linear system is the maximum singular value of its complex gain over frequency. It is also the maximum amplification when considering the $\mathcal{L}_2$ norm on signals. For a system $G(s)$ of input $u(t)$ and output $y(t)$, $||G(s)||_\infty = \max_{\omega\in\mathbb{R}} \overline{\sigma}(G(j\omega)) = \max_{u(t)} \frac{||y(t)||_2}{||u(t)||_2}$.

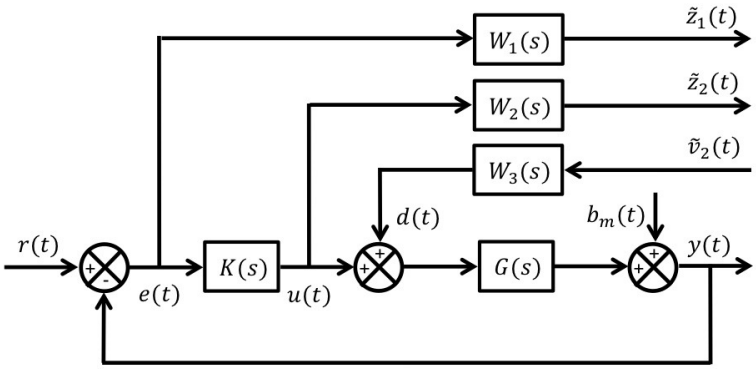

Figure 11. Design scheme with the weighting filters $W_1(s)$, $W_2(s)$ and $W_3(s)$ for the $\mathbf{H}_\infty$ synthesis

for both forces and moments. The weighting filters $W_1(s)$, $W_2(s)$ and $W_3(s)$ are chosen under the shape $W_k(s) = \text{diag}(w_{k1}(s)\,\mathbb{I}_{3\times3}, w_{k2}(s)\,\mathbb{I}_{3\times3})$, where the SISO weighting filters $w_{k1}(s)$ correspond to the positions or forces and $w_{k2}(s)$ corresponds to the orientations or moments. The weighting filters were tuned to achieve the requested closed-loop performances, resulting in:

$$\begin{cases} w_{11}(s) &= 0.5 \\ w_{21}(s) &= \left(250\,\dfrac{s+10^{-2}}{s+10^4}\right)^2 \\ w_{31}(s) &= 10\,\dfrac{s+10}{s+10^4} \end{cases} \qquad \begin{cases} w_{12}(s) &= 0.5 \\ w_{22}(s) &= \left(100\,\dfrac{s+10^{-2}}{s+10^4}\right)^2 \\ w_{32}(s) &= \dfrac{s+10}{s+10^4} \end{cases} \tag{24}$$

Notice that the more simple two-bloc scheme, based on weighting filters $W_1(s)$ and $W_2(s)$ only, was not sufficient to reject the disturbances induced by the non-linear behaviour of the system.

The frequency response of the controller (singular values) is given in Fig. 12. For both position and orientation, the controller exhibits a high gain in low frequencies that favors the disturbance rejection, then the gain increases in the medium frequencies, bringing phase to allow a high bandwidth and finally decreases in the high frequencies, thus reducing the effects of the measurement noise.

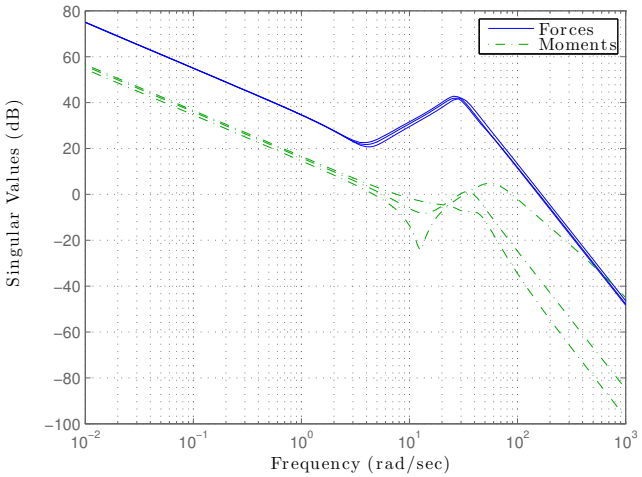

Figure 12. Singular values of the $\mathbf{H}_\infty$ position controller $K(s)$

Figure 13 shows the singular values of the closed-loop transfer functions of interest involved in the $\mathbf{H}_\infty$ synthesis and their corresponding templates. The resolution has been done with the Riccati method. The obtained value of $\gamma = 0.92$ being slightly smaller than 1, the templates are fully satisfied and the tracking trajectories performances slightly exceed those intended with a bandwidth of 6 rad/s for position and of 2 rad/s for orientation, a modulus margin of 0.57 for position and of 0.61 for orientation and a static error less than 1 % on position and orientation (see Fig. 13(a)).

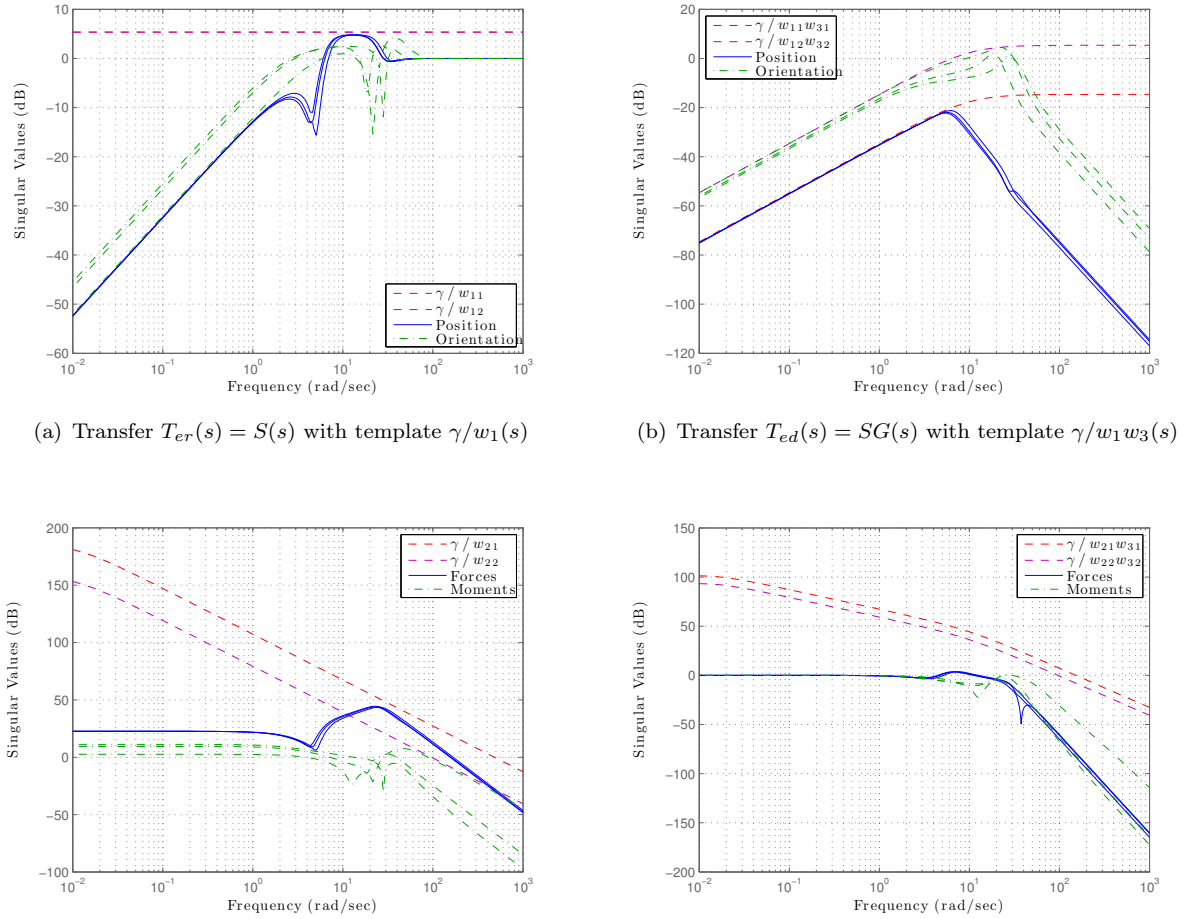

(a) Transfer $T_{er}(s) = S(s)$ with template $\gamma/w_1(s)$

(b) Transfer $T_{ed}(s) = SG(s)$ with template $\gamma/w_1 w_3(s)$

(c) Transfer $T_{ur}(s) = KS(s)$ with template $\gamma/w_2(s)$

(d) Transfer $T_{ud}(s) = KSG(s)$ with template $\gamma/w_2\, w_3(s)$

Figure 13. Singular values of the closed-loop transfer functions of interest $T_{z_k v_l}(s)$ and their corresponding templates $\gamma/W_{ik}(s)\, W_{ol}(s)$

5.2 *Tension distribution*

5.2.1 Problem statement and state of the art

The wrench F_{ev} computed by the $\mathbf{H}_\infty$ controller must be converted into motor current vector I_m^*. This requires to solve the system of linear equations (13) under the inequality constraints (11), in order to ensure that the cable tension vector T remains inside the interval $[T_{\min}\ T_{\max}]$. Due to the actuation redundancy, the system of equations (13) is under-determined and then has an infinity of solutions (assuming that W_I has full rank $r = n - m$). This can be exploited to minimise the distance towards some objective value I_{obj} corresponding to an objective tension vector T_{obj}. This

is done by solving the quadratic optimisation problem of the objective function $E(I_m^*, \lambda)$ given by:

$$E(I_m^*, \lambda) = \frac{1}{2} (I_m^* - I_{\text{obj}})^T (I_m^* - I_{\text{obj}}) + (F_{ev} - W_I \, I_m^*)^T \, \lambda \tag{25}$$

where $\lambda \in \mathbb{R}^m$ is the Lagrange multiplier associated to the equality constraints $F_{ev} - W_I \, I_m^* = 0$. The solution writes:

$$I_m^* = I_{mp}^* + I_{mn}^* \tag{26}$$

where:

- I_{mp}^*, the particular solution that minimises the norm of $I_m^* - I_{\text{obj}}$, acts on the end-effector pose:

$$I_{mp}^* = W_I^+(X_e) \, F_{ev} \tag{27}$$

  with $W_I^+ = W_I^T \, (W_I \, W_I^T)^{-1}$ the Moore-Penrose pseudo-inverse of the wrench matrix W_I.
- I_{mn}^*, the homogeneous solution of W_I null-space, acts on the tensions, without effect on the end-effector pose:

$$I_{mn}^* = [\mathbb{I}_{n \times n} - W_I^+(X_e) \, W_I(X_e)] \, I_{\text{obj}} \tag{28}$$

A number of approaches are available in the literature for the determination of the objective tension vector T_{obj} that maintains the cable tension vector T inside a feasible tensions workspace. The available works can be classified in two categories. The first approach opted for iterative algorithms, so that efficient constrained optimisation methods can be used such as Linear Programming Methods (LPM) (Gosselin and Grenier, 2011; Ming and Higuchi, 1994; Oh et Agrawal, 2005), but the cable tension continuity is not guaranteed. Other optimisation methods are also used such as Non-Linear Programming Methods (NLPM) in the particular case of Quadratic Programming Methods (QPM) (Oh et Agrawal, 2005; Vafaei et al., 2010), and the general NLPM with the gradient descent method to solve the problem in a quadratic formulation (Gholami et al., 2008). These quadratic methods guarantee the tensions continuity but have a non-predictable runtime, which is a drawback for real-time implementation. The second approach relies on non-iterative algorithms to handle the real-time control constraints. For instance, Mikelsons et al. (2008) proved that the Center of Gravity (CoG) of the feasible tension distribution workspace (the set of solutions of equations (13) satisfying the tension constraints (11)) is a solution that ensures the tensions continuity. Recently, Gouttefarde et al. (2015) have proposed contributions to improve the CoG method to the case of two degrees of redundancy.

5.2.2 Considered algorithm

The proposed approach is inspired from the algorithm proposed by Lafourcade (2004) appropriate to satisfy real-time constraints (currently less than 1 ms). It has been improved to account for the motor dynamics (9) by considering a variable I_{obj} and accounting for the current limits of the motors. It consists in:

(1) selecting T_{obj} inside the feasible tension workspace and calculating I_{obj} from Eqn. (9) by considering $T = T_{\text{obj}}$ and solving in $I_{\text{obj}} = I_m$;
(2) computing the current reference I_m^* that satisfies constraints (13) while minimizing the mean-square error on $I_m^* - I_{obj}$ without considering the tension inequalities constraints (11) as given by (27);

(3) if some inequality constraints on the tensions are violated, then q concerned inequalities selected among them are transformed into equality constraints on the currents (not more than r tension inequality constraints can be saturated simultaneously) and included into the optimisation problem. All combinations of 1 to r violated tension inequality constraints are considered until one solution is met that satisfies all the non-saturated tension inequalities constraints. The process is repeated until a feasible solution is met. If no solution is found, the vector I_{obj} can be scaled by a scalar factor without impact on the trajectory. If the problem has no solution, the reference trajectory must be decelerated.

More precisely, for a combination of q tension constraints, the current vector I_m^* is obtained by solving the new quadratic optimisation problem of the objective function $E_{\text{sat}}(I_m^*, \lambda, \mu)$ given by:

$$E_{sat}(I_m^*, \lambda, \mu) = \frac{1}{2} \left(I_m^* - I_{obj}\right)^T \left(I_m^* - I_{obj}\right) + \left(F_{ev} - W_I \; I_m^*\right)^T \lambda + \left(S^T \; I_m^* - I_{\text{sat}}\right)^T \mu \tag{29}$$

where:

- the selection matrix $S = [s_1 \; \ldots \; s_q] \in \mathbb{R}^{n \times q}$ concatenates the vectors s_k of the canonical basis of $\mathbb{R}^n$ to select the combinations of the violated tension constraints to be saturated,
- the vector $\mu \in \mathbb{R}^q$ is the Lagrange multiplier associated to the current equality constraints $S^T \; I_m^* - I_{\text{sat}} = 0$, such as the vector $I_{\text{sat}} \in \mathbb{R}^q$ is the current vector that corresponds to the saturated tension vector T_{sat} and is calculated from Eqn. (9).

The solution of the optimisation problem (29) writes:

$$I_m^* = I_{mp}^* + I_{mt}^* \tag{30}$$

where:

$$I_{mt}^* = I_{mn}^* + \left[W_I^+(X_e) \; W_I^{\text{sat}}(X_e) - S\right] \; \left[S^T \; W_I^+(X_e) \; W_I^{\text{sat}}(X_e) - \mathbb{I}_{q \times q}\right]^{-1} \; \triangle_{\text{sat}} \tag{31}$$

in which the resulting saturated wrench matrix is $W_I^{\text{sat}}(X_e) = W_I(X_e) \; S$, and the vector of the excessive motor currents $\triangle_{\text{sat}} = I_{\text{sat}} - S^T \; (I_{mp}^* + I_{mn}^*)$ is an image of the excess in cable tensions evaluated from Eqn. (9).

5.3 *Experiments*

5.3.1 Evaluation tasks

A set of trajectories have been chosen in order to evaluate the performance of the controlled system. Starting from the center of the workspace identified by a null position and orientation, the trajectory is composed of steps: the end-effector is requested to follow the edges of a square centred into the workspace, belonging to the plane (X_o, Y_o) and of width 0.2 m.

The feasible tension workspace is defined by the boundaries $T_{\min} = 1.48$ N and $T_{\max} = 18.5$ N (the maximum tension supported by the cables being of 247 N), which have been calculated based on the static model of the actuators, considering the limits of the motor currents $I_{\min} = 0$ A and $I_{\max} = 3$ N, and the limits of the unwinding cable lengths $L_{\min} = 0$ m and $L_{\max} = 4.82$ m. The objective tension vector is chosen as $T_{\text{obj}} = 10$ N.

5.3.2 Results

The experimental results obtained with the square trajectory are reported in Fig. 14. One can notice that the position is properly controlled in a decoupled fashion (Fig. 14.a), while the currents

(Fig. 14.b) and tensions (Fig. 14.c) remain inside the prescribed workspace and the tensions are close to $T_{\text{obj}} = 10$ N. The cables tensions have been estimated using the dynamic model of the actuators (9).

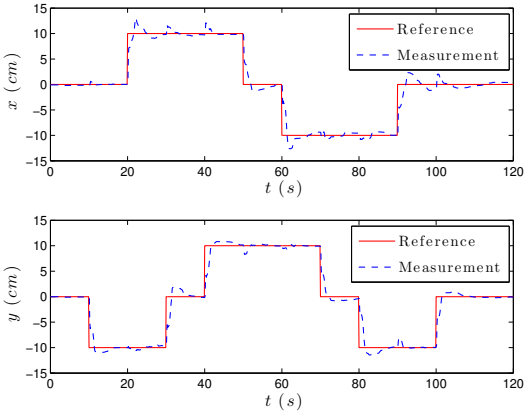

(a) Platform position (x and y coordinates): reference and measurement

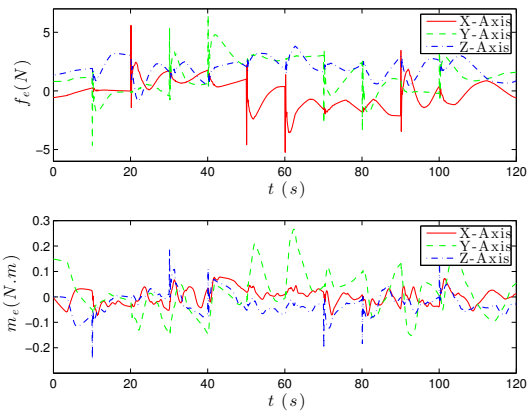

(b) Control signals: force f_e and moment m_e

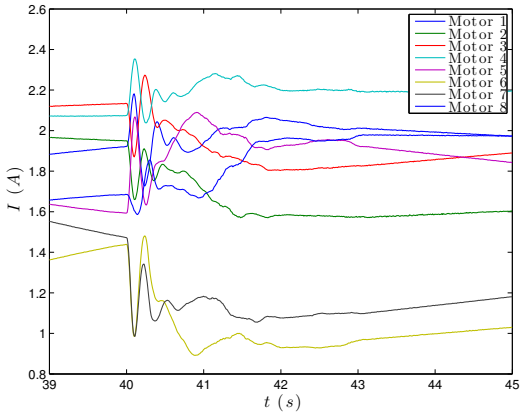

(c) Measured currents

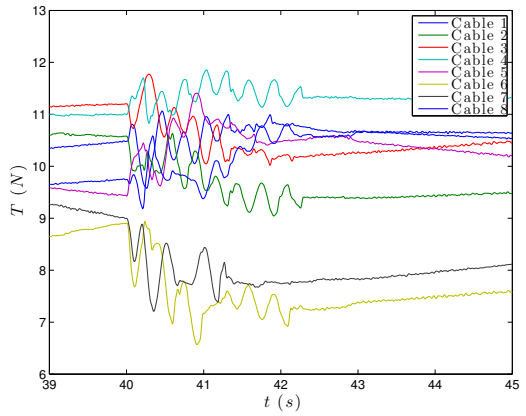

(d) Estimated tensions

Figure 14. Experimental results with the $\mathbf{H}_\infty$ position controller

Simulation results provided in Fig. 14 include Coulomb frictions that were found as a major source of misfit between the simulated and the measured signals. As shown in Fig. 15, the prediction provided by the model is much more accurate as soon as Coulomb friction is included.

6. Conclusion

This paper is a methodological contribution for the identification and control of 6-DoF CDPRs. First, a two-step identification methodology has been proposed to estimate sequentially the combined kinematic and dynamic parameters of 6-DoF CDPRs. The method has been successfully implemented on the INCA 6D robot, allowing to improve the input-output behaviour of the model, as shown by the good fit on the motor positions. Moreover, the estimated values of both kinematic and dynamic parameters remain close from their initial guessed values, except for the viscous friction term. The validity of the identified model remains satisfying even when the cables are subject to non-negligible vibrations, as could be observed on the validations with faster trajectories. Then, an $\mathbf{H}_\infty$ methodology has been proposed for the vision-based position control of 6-DoF CDPRs, which

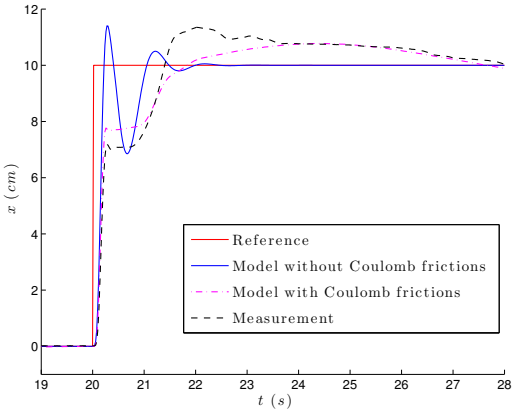

Figure 15. Effect of Coulomb friction on $\mathbf{H}_\infty$ position controller: the comparison of step responses on models with and without Coulomb friction and on the experimental system validate the sensitivity of the closed-loop system with respect to Coulomb friction

has been then implemented to the INCA 6D robot. The simulation and experiment results have shown that the $\mathbf{H}_\infty$ position controller combined with the tension distribution algorithm allows good bandwidth, accuracy and disturbance rejection, while maintaining the cables under feasible tensions. Notice that strong disturbance rejection properties had to be conferred to the controller in order to dominate the non-linear behaviour of the system. One strong limitation of the $\mathbf{H}_\infty$ methodology is that it leads to a LTI controller that is restricted to a neighborhood of the nominal position. However, the robustness of the designed controller was sufficient for an evolution in a reasonably large domain. For a larger workspace, gain-scheduling techniques would be fruitful to adapt the controller behaviour.

References

P. Apkarian and D. Noll. Nonsmooth H_∞ synthesis. *IEEE Transactions on Automatic Control*. vol. 51, no. 1, p. 71-86, 2006

J. Burke, D. Henrion, A. Lewis and M. Overton. HIFOO - a Matlab package for fixed-order controller design and $\mathbf{H}_\infty$ optimisation. *IFAC Symposium on Robust Control Design*, 2006

M. Carricato and J-P Merlet. Direct geometrico-static problem of under-constrained cable-driven parallel robots with three cables. *Int. Conf. Robotics and Automation (ICRA)*, p. 3011-3017, 2011

N. Dagalakis, J. Albus, B-L. Wang, J. Unger and J. Lee. Stiffness study of a parallel link robot crane for shipbuilding applications. *Journal of Offshore Mechanics and Arctic Engineering*, vol. 111, no 3, 183-193p. 183-193, 1989

T. Dallej, M. Gouttefarde, N. Andreff, M. Michelin and P. Martinet. Towards vision-based control of cable-driven parallel robots. *IEEE/RSJ Int. Conf. Intelligent Robots and Systems (IROS)*, p. 2855-2860, 2011

T. Dallej, M. Gouttefarde, N. Andreff, R. Dahmouche and P. Martinet. Vision-based modeling and control of large-dimension cable-driven parallel robots. *IEEE/RSJ Int. Conf. Intelligent Robots and Systems (IROS)*, p. 1581-1586, 2012

J. Dolye, K. Glover, P. Khargonekar and B. Francis. State-space solutions to standard $\mathbf{H_2}$ and $\mathbf{H}_\infty$ control problems. *IEEE Trans. Autom. Control*, vol. 34, no 8, p. 831-847, 1989

G. Duc and S. Font. Commande $\mathbf{H}_\infty$ et μ-analyse. Hermès Science Publications, 1999

P. Gahinet and P. Apkarian. A linear matrix inequality approach to $\mathbf{H}_\infty$ control. *Int. J. Robust Nonlin. Control*. vol. 4, no 4, p. 421-448, 1994

M. Gautier and P. Poignet. Identification en boucle fermée par modèle inverse des paramètres physiques de systèmes mécatroniques. *J. Européen des Systèmes Automatisés*, vol. 36, no 3, p. 465-480, 2002

M. Gautier, A. Janot and P. Vandanjon. A new closed-loop output error method for parameter identification

of robot dynamics. *IEEE Transactions on Control Systems Technology*, vol. 21, no 2, p. 428-444, 2013

P. Gholami, M. Aref, and H. Taghirad. On the control of the KNTU CDRPM: A cable driven parallel manipulator. *IEEE/RSJ Int. Conf. Intelligent Robots and Systems (IROS)*, p. 2404-2409, 2008

M. Gouttefarde, J. Lamaury, C. Reichert, T. Bruckmann. A Versatile Tension Distribution Algorithm for n -DOF Parallel Robots Driven by n+2 Cables, *IEEE Transactions on Robotics*, vol. 31, no 6, p. 1444-1457, 2015

C. Gosselin. Global planning of dynamically feasible trajectories for three-DoF spatial cable-suspended parallel robots. *Cable-Driven Parallel Robots*, Springer, 2012

C. Gosselin and M. Grenier. On the determination of the force distribution in overconstrained cable-driven parallel mechanisms. *Meccanica*, vol. 46, no 1, p. 3?15, 2011

A. Janot, M. Gautier, A. Jubien and P. Vandanjon. Comparison between the CLOE method and the DIDIM method for robots identification. *IEEE Transactions on Control Systems Technology*, vol. 22, no 5, p. 1935-1941, 2014

O. Kanoun, F. Lamiraux and P.B. Wieber. Kinematic Control of Redundant Manipulators: Generalizing the Task-Priority Framework to Inequality Task. *IEEE Transactions on Robotics*, vol. 27, n° 4, p. 785-792, 2011

S. Kawamura, H. Kino, and C. Won. High-speed manipulation by using parallel wire-driven robots. *Robotica*, vol. 52, no 2, p. 13-21, 2000

W. Khalil and E. Dombre. Modélisation, identification et commande des robots. Hermès - Lavoisier, 1999

P. Lafourcade. Etude des manipulateurs parallèles à câbles, conception d'une suspension active pour soufflerie. Ph. D. Thesis, ENSAE School, 2004

J. Lamaury, M. Gouttefarde, M. Michelin and O. Tempier. Design and control strategies of a redundant suspended cable-driven parallel robot. *Advances in Robot Kinematics (ARK)*, J. Lenarcic and M. Husty eds., Springer, p. 237-244, 2012

E. Laroche, R. Chellal, L. Cuvillon and J. Gangloff. A preliminary study for $\mathbf{H}_\infty$ control of parallel cable-driven manipulators. *First Int. Conf. on Cable-Driven Parallel Robots*, T.Bruckmann and A. Pott, eds. Cable-Driven Parallel Robots, Springer, p. 353-369, 2012

J-P. Merlet. Les robots parallèles. Hermès - Lavoisier, 1997

L. Mikelsons, T. Bruckmann, M. Hiller and D. Schramm. A real-time capable force algorithm for redundant tendon-based parallel manipulators. *IEEE Int. Conf. Robotics and Automation (ICRA)*, p. 3869-3874, 2008

A. Ming and T. Higuchi. Study on multiple degree-of-freedom positioning mechanism using wire-concept, design and control (part 1). *Int. J. of the Japan Society for Precision*, vol. vol. 28, no 2, p. 131-138, 1994

S. Oh and et S. Agrawal. Cable suspended planar robots with redundant cables: controllers with positive tensions. *IEEE Trans. Robot.*, p. 457-465, 2005

P. Poignet, N. Ramdani and O. Vivas. Robust estimation of parallel robot dynamic parameters with interval analysis. *IEEE Conf. on Decision and Control*, 2003

P. Renaud, A. Vivas, N. Andreff, P. Poignet, P. Martinet, F. Pierrot and O. Company. Kinematic and dynamic identification of parallel mechanisms. *Control Engineering Practice*, vol. 14, n°9, p. 1099-1109, 2006

A. Trevisani. Experimental validation of a trajectory planning method avoiding cable slackness and excessive tension in under-constrained translational planar cable-driven robots. *Cable-Driven Parallel Robots*, Springer, 2012

A. Vafaei, M. Aref and H. Taghirad. Integrated controller for an over constrained cable driven parallel manipulator: KNTU CDRPM. *IEEE Int. Conf. on Robotics and Automation (ICRA)*, p. 650-655, 2010

P. Vischer and R. Clavel. Kinematic calibration of the parallel Delta robot. *Robotica*, vol. 16, p. 207-218, 1998

E. Walter and L. Pronzato. *Identification of Parametric Models from Experimental data*, Springer-Verlag, 1997

D. Yu, W. Chen and H. Li. Kinematic parameter identification of parallel robots for semi-physical simulation platform of space docking mechanism. *Mechanics*, vol. 17, no 5, p. 2029-6983, 2011